International Journal of Heat and Mass Transfer 125 (2018) 1296–1309

Contents lists available at ScienceDirect

International Journal of Heat and Mass Transfer

journal homepage: www.elsevier.com/locate/ijhmt

Machine learning classification of boiling regimes with low speed, direct and indirect visualization

Gustavo M. Hobold, Alexandre K. da Silva *

Department of Mechanical Engineering, Federal University of Santa Catarina, Florianopolis, SC 88040-900, Brazil

ARTICLE INFO

Article history:
Received 18 October 2017
Received in revised form 28 April 2018
Accepted 30 April 2018
Available online 16 May 2018

Keywords:
Pool boiling
Film boiling
Machine learning
Boiling regimes
Visualization

ABSTRACT

Multiphase flow pattern identification is of utmost importance to the energy industry, given that thermohydraulic operating conditions are drastically affected by flow and heat transfer regimes. In industrial boilers and nuclear reactors, for instance, the heat transfer coefficient – and hence the heater temperature – is significantly affected by the boiling regime, where the onset of film boiling can be catastrophic to the equipment and cause irreparable damage. In this paper, it is shown that a machine can learn from visualization and successfully classify and separate natural convection, nucleate boiling and film boiling regimes using low speed and low resolution image frames acquired from visualization of an on-wire pool boiling experimental setup (direct visualization) even when only the departed, ascending bubbles are considered – i.e., the heater is suppressed from the image (indirect visualization). While not the main objective of this paper, principal component analysis of the frames is shown to provide information regarding bubble dynamics and hence is used for dimensionality reduction. Two types of classifiers, namely support vector machines and neural networks, are shown to be able to classify pool boiling frames with over 93% accuracy sufficiently fast, possibly enabling real-time execution and classification, even during indirect visualization and, hence, providing a non-intrusive and low-cost pool boiling regime identification.

© 2018 Elsevier Ltd. All rights reserved.

1. Introduction

Algorithms that learn from data have been gaining momentum as computational power has significantly increased during the past few decades. Various problems have been tackled with artificial intelligence derived from machine learning, often producing algorithms that excel human performance in various tasks. For instance, machines can outperform humans in a variety of complex board games, such as chess [1] and, more recently, Go [2]. Machine learning has also been used in conjunction with computer vision for automated, self-driving cars [3] and facial and object recognition [4]. Deep learning algorithms have also been devised to produce physician-level disease identification [5]. More specifically with respect to the physical sciences, machine learning has been described as a potential super-tool for research assistantship [6], with a potential impact similar to other computational techniques such as CFD. Recently, machine learning has been utilized to automatically detect phases of matter in highly complex disordered lattices [7], polymer states [8], to model turbulence [9], predict solar radiation incidence [10], as well as in flow field reconstruction [11].

It is well known that multiphase flow patterns strongly influence the performance of thermohydraulic systems. For instance, pressure gradients in multiphase flow have been shown to be strongly influenced by flow regime [12], and high speed visualization studies have assisted in understanding transition between regimes [13]. In general, visualization studies assist in building flow pattern maps [13,14] as well as in identifying heat transfer enhancement or deterioration mechanisms [15]. Additionally, while still largely unexplored, machine learning techniques have been used in conjunction with pressure sensor data to identify multiphase flow regimes [16–18], but as to the authors best of knowledge, with no assistance from visualization.

Particularly with respect to boiling heat transfer, four regimes can be usually detected: natural convection, nucleate boiling, transition boiling and film boiling [19]. In general, evaporating heat exchangers operate in the nucleate boiling regime due to higher heat transfer coefficients, and because the onset of film boiling can often be catastrophically destructive. Therefore, avoiding film boiling is of major concern. Various techniques have been devised to avoid film boiling. For instance, nanofluids have been extensively studied as a way to increase critical heat flux [20–23], which, due to nanoparticle deposition on the heater's surface, results in increased wettability [24]. Graphene oxide-based solutions have

* Corresponding author.
E-mail address: a.kupka@ufsc.br (A.K. da Silva).

https://doi.org/10.1016/j.ijheatmasstransfer.2018.04.156
0017-9310/© 2018 Elsevier Ltd. All rights reserved.

Nomenclature

f	frequency [Hz], factor [–]
g	acceleration due to gravity [m/s^2]
h	histogram distribution [–]
x	data sample [–]
D	departure diameter [m]
F	F-score [–]
K	number of features [–]
L	luminance [–]
M	set size [–]
N	number [–]
P	precision [–]
R	recall [–]
S	cross-entropy [–]
U	number of units per layer [–]
V	retained variance ratio [–]
W	number of layers [–]
X	dataset [–]

Greek

ρ	density [kg/m^3]
σ	surface tension [N/m]
λ	eigenvector [–]
Λ	matrix of eigenvectors [–]

Subscript

d	bubble departure
ds	downsampling
l	liquid
i	index
j	index
p	pixels
v	vapor
A	active nucleation sites, acquisition

Superscript

‘	modified
N	number of bins

Acronyms

ANN	artificial neural network
CFD	computational fluid dynamics
DSLR	digital single-lens reflex
DR	dimensionality reduction
FB	film boiling
LED	light-emitting diode
MLPNN	multi-layer perceptron neural network
NB	nucleate boiling
NC	natural convection
NN	neural network
PCA	principal component analysis
ReLU	rectified linear unit
SSI	structural similarity index
SVM	support vector machine

also been shown to delay the onset of critical heat flux, by significantly increasing the transition time [25]. Others have suggested directly texturing heater surfaces to increase capillarity and hence delay film boiling [26–30]. However, while many studies focus on increasing critical heat flux and heat transfer coefficient, fewer tools exist that are capable of rapid and automatic boiling regime detection. In addition, the most common one, i.e., heater temperature measurement, is often based on an intrusive method that requires the placement of a temperature sensor very close to the heater surface, as commonly done in experimental setups.

Visualization studies have been capable of detecting significant difference between natural convection, pool boiling, transition boiling and film boiling regimes. For instance, the Zuber model for critical heat flux prediction is reportedly based on visualization studies of Taylor and Kelvin-Helmholtz instabilities that ultimately result in the boiling crisis [31]. More recent studies have also been conducted to understand the heat transfer mechanisms in both film and nucleate boiling regimes [30,32,33]. However, those results are usually conducted with the assistance of a high-speed camera, which is generally expensive, and, particularly with respect to the utilization of machine learning in image processing, might lead to unnecessary highly correlated frame sequences and potentially introduce significant bias to the identification process, as will be shown along the paper. Additionally, real-time image processing and classification in miniaturized and compact systems may require full functionality of boiling regime identification operating with low speed and low resolution data.

Given the importance of boiling regime identification and the existence of visualization patterns that distinguish natural convection, nucleate boiling and film boiling, the present paper deploys image processing and machine learning techniques to classify pool boiling regimes. It is shown that low speed and low resolution visualization, coupled to either support vector machines or neural networks, can successfully identify pool boiling regimes. It is demonstrated that low speed visualization is not only desirable, but also necessary to obtain uncorrelated images to train the learning algorithms. Moreover, through a dimensionality reduction analysis, it is demonstrated that the algorithms can be trained with low resolution images without significant loss of dataset variance or entropy gain. A principal component analysis (PCA) is performed on the training set, which is able to identify eigenfigures capable of capturing the variance of the boiling process, which can be correlated with on-wire bubble dynamics and bubble departure diameter. While the objective of this paper is not an in-depth analysis of boiling heat transfer physics, it is shown that PCA can potentially be used to identify key features of the boiling process, such as on-wire bubble dynamics. Then, two classification algorithms are trained on low-dimensional data, which shows that trained support vector machines and neural networks are capable of correctly detecting pool boiling regimes with up to over 94% precision. Given the short prediction times and generally low computational cost of the proposed algorithms, combined with low resolution and low frequency visualization, it is expected that the methodology proposed in this paper can be embarked on and executed by compact hardware and allow inexpensive non-intrusive multiphase regime detection.

2. Methodology flowchart

In general, supervised learning algorithms, such as the neural networks and support vectors machines that will be used in this paper, are trained by labeled data, i.e., a data sample that comes with its specific class label. Both the label (natural convection, nucleate boiling, and film boiling) and the data sample (frame) are supplied to the algorithm, which is then trained using conventional optimization techniques. However, before training, several analyses can be performed on the dataset to reduce the

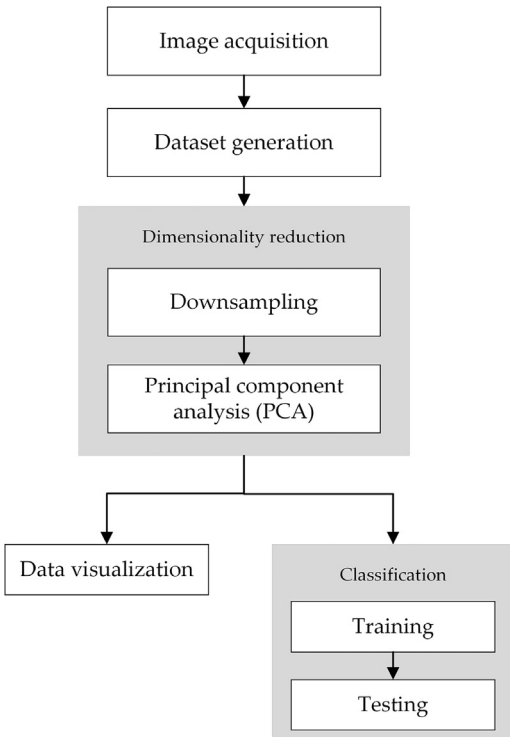

Fig. 1. Methodology flowchart.

dimensionality of the problem. A flowchart illustrating the analysis sequence proposed in the present work is shown in Fig. 1. First, a description of data and image acquisition process is presented in Section 3, along with dataset construction. The utilization of low-speed visualization is then justified in Section 4. Section 5 reports dimensionality reduction (DR) and feature selection, where Section 5.1 discusses DR by downsampling and Section 5.2 discusses DR and feature selection by principal component analysis (PCA). Then, a discussion of how PCA can be used for dataset visualization is presented in Section 6. Finally, Section 7 shows that the utilization of conventional machine learning classifiers can be used to interpret and identify boiling regimes from image data, discussing classification performance and time per prediction.

3. Data acquisition and labeling

The experimental apparatus consists of a boiling chamber made from a borosilicate glass body with an internal diameter of 144 mm and length of 200 mm as shown in Fig. 2a. Two electrolytic copper electrodes connect a 450 μm diameter Nichrome wire with an approximate length of 60 mm, which dissipates heat to a pool of deionized water by Joule effect. Electrical current is provided by a DC power supply and measured by the voltage drop over a current sense shunt resistor (MRS137513-1, Vishay Dale). During the experiment, two 750 W heaters control the bulk fluid temperature, which is measured by a RTD, in such a way that the water remains saturated. The boiling chamber is open to the atmosphere, where a transducer measures the pressure. Video is acquired by a conventional DSLR camera (D3100, Nikon) equipped with a 30–55 mm lens at 30 Hz and at a resolution of 1280 × 720 pixels (720p) – see Fig. 2b. Measurement data is acquired by an Agilent 34972A at approximately every 3 s. An Arduino UNO synchronizes the data acquisition software with image data through LED signaling. Data processing is done in Python, using various scientific computing packages (SciPy/NumPy [34], Matplotlib [35], scikit-image [36], scikit-learn [37]).

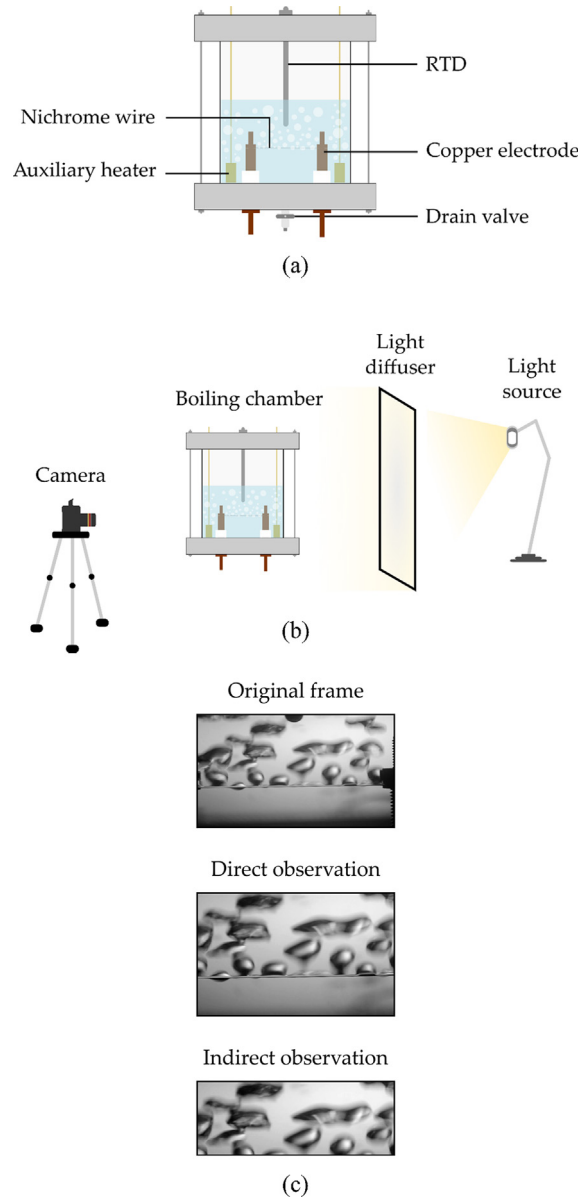

Fig. 2. (a) Boiling chamber along with its main components and (b) experimental set-up for visualization and (c) examples of direct and indirect observation frames.

Each video frame is composed of 1280 pixels in width by 720 pixels in height, totaling 921,600 pixels. Images are acquired in RGB and, hence, each pixel is an integer vector of three components, each ranging from 0 to 255. All frames are nearly identically cropped in order to remove unnecessary background, such as the copper electrodes or signaling LEDs. Fig. 2c shows an example of an original frame and a cropped one. In addition to cropping, each frame is randomly dislocated by, at most, 80 pixels both vertically and horizontally so that the training data is not insensitive to slight view point deviations. In order to guarantee that the results are not overly dependent on a single acquisition sequence, two experimental runs are performed using different Nichrome wires of the same diameter at an increasing current of approximately 9 W $(cm^2\ min)^{-1}$, from 2 W/cm^2 to wire failure.

After acquisition, each video was converted to image sequences and labelled as natural convection, nucleate boiling or film boiling. The transition from natural convection to nucleate boiling was visually detected by observing the first nucleation site. The transition from nucleate to film boiling was identified visually and was

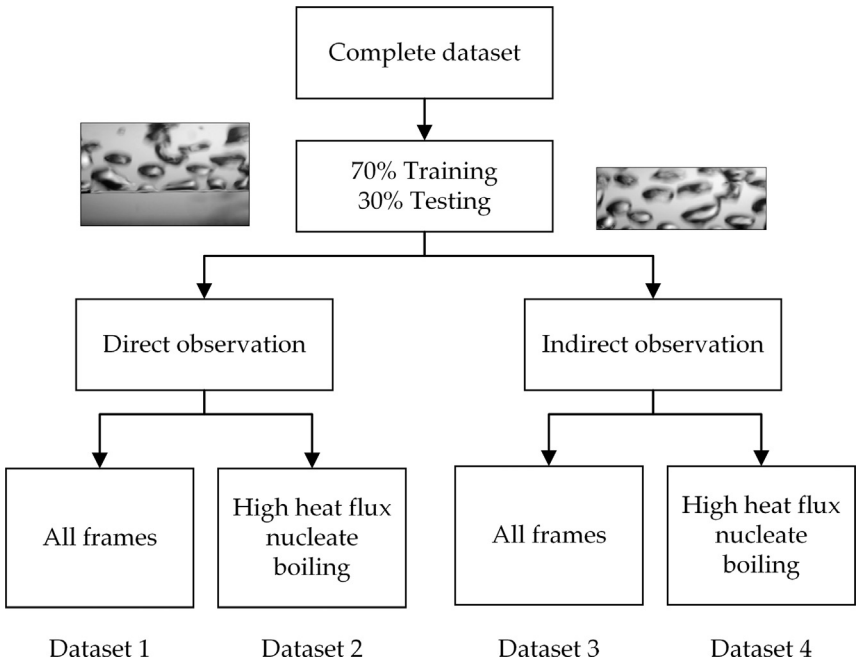

Fig. 3. Datasets used in the paper.

based on resistance measurements – wire resistance increased by over 10% during the transition. All frames that were captured for a heat flux lower than that for which the first activated nucleate boiling site was observed were labeled as natural convection (NC). All frames that occurred after a significant increase in wire resistance – a result of temperature increase due to the onset of film boiling – were labeled as film boiling (FB). And finally, all frames associated with heat fluxes higher than the onset of nucleate boiling and lower than the critical heat flux were labeled as nucleate boiling (NB). After labelling, heat flux and resistance measurements were no longer used and the machine learning algorithms – including the classifiers – had no access to it.

3.1. Datasets

After labeling, two sets of data were created, to which frames were randomly assigned. The larger one, comprising 70% of all frames, was used for training the different learners that will be presented in this paper. The remaining 30% comprise the test set, which is used to obtain quantitative information on how well the classifiers are able to perform on pool boiling regime data that was not used for training. Once the training and test sets are defined, these were duplicated into two additional subsets. One subset comprised the original frames, which includes wire visualization, namely direct observation, and another that contained the same frames but from which the wire was cropped – this image sequence was named indirect observation. The justification for indirect observation lays on the fact that direct heated surface observation may not be always available or its observation may induce non-negligible bias to the learning algorithm – for instance, surfaces during film boiling of water tend to emit significant radiation in the visible spectrum, leading to high pixel intensity that is not directly related to bubble dynamics. Hence, it's worth exploring whether it is possible to learn from indirect observation, i.e., observing only the departed bubbles.

Finally, 2207 natural convection, 29,986 nucleate boiling and 4346 film boiling frames composed each dataset, of which, as discussed, approximately 70% of each class were used for training, and the remaining 30% were used for testing. Fig. 3 shows a scheme that more clearly depicts the different datasets that were considered.

4. Image correlation and low speed visualization

High speed visualization is a common tool used in the analysis of boiling heat transfer due to the fast, transient bubble dynamics during nucleation, growth and departure, which is usually faster than what the usual 30 Hz digital camera is capable of capturing. In fact, the bubble departure frequency can be scaled as [31]

$$f_d \sim \frac{1}{D}\left[\sigma g\left(\frac{\rho_l - \rho_v}{\rho_l^2}\right)\right]^{1/4} \tag{1}$$

where D is the bubble departure diameter, σ is the liquid-vapor surface tension, g is the acceleration due to gravity, ρ_l is the liquid density, and ρ_v is the vapor density. For instance, for pure saturated water at atmospheric pressure and Earth gravity, bubble departure diameter has been reported to be between 1 and 10 mm, and departure frequency is usually between 20 and 40 Hz. Hence, studies focusing on bubble dynamics conduct visualization studies in frequencies of, at least, several times higher than f_d. The result of high speed visualization would, then, be a sequence of consecutive frames that are highly correlated with each other in order to be able to infer on the intrinsic relationship between the images and the physical phenomenon.

However, the objective of this paper is not to conduct a bubble dynamics analysis, but rather to use machine learning to identify boiling regimes. In doing so, a large amount of uncorrelated image data should be fed to the learner (i.e., classifier) in order to train it. Therefore, if the acquisition frequency is f_A, then

$$f_A < f_d N_A \sim \frac{N_A}{D}\left[\sigma g\left(\frac{\rho_l - \rho_v}{\rho_l^2}\right)\right]^{1/4} \tag{2}$$

where N_A is the number of active nucleation sites captured by the camera, which generally increases as the degree of superheating increases [31]. Hence, low speed visualization combined with a large captured area is, in fact, a desirable feature in the kind of study that will be performed in this paper.

The correlation between images acquired at low speed and images acquired at high speed can be illustrated as follows. Consider, for instance, the structural similarity index (SSI) [36,38], which is unitary when two images are equal (i.e., completely correlated) and zero if they are completely uncorrelated. Consecutive frames acquired by high speed visualization are, therefore, expected to have very high average structural similarity index. More importantly, when visualizing the resulting distribution of SSI of consecutive images over a particular interval, it's expected that the resulting distribution will be heavily skewed towards unity. In fact, this result was verified by analyzing high speed visualization data. However, when training a classifier, it is necessary that all data be uncorrelated, given that otherwise the learner will be biased towards the dataset on which it was trained.

On the other hand, the distribution of structural similarity index between consecutive images in low speed visualization is expected to be Gaussian, given that consecutive frames are mostly uncorrelated. Therefore, consider now images acquired by a conventional DSLR camera (Nikon D3100) at 30 frames per second (i.e., low speed visualization) of the heated wire during nucleate boiling. Because the number of active sites of nucleation is estimated to be on the order of 10^1, then $N_A f_d$ is much higher than $f_A = 30\ Hz$. Hence, as can be seen in Fig. 4a, there is no discernible pattern in the structural similarity index, which is nearly constant apart from random noise. In fact, as shown in Fig. 4b the histogram distribution of SSI shows that the distribution is nearly Gaussian and, hence, the images may be interpreted as completely uncorrelated. In fact, by performing a normality test on the structural index data using the Shapiro-Wilk normality test, which determines whether the data is likely to have been withdrawn from a Gaussian distribution [39], the p-value of the low correlation data is 0.58, whereas the p-value of high-speed data is as low as 10^{-23}. Additionally, normality was also verified by plotting the SSI distribution against a fitted Gaussian distribution, which is known in statistics as a quantile-quantile plot.

Therefore, low speed visualization is encouraged for boiling regime classification not only from a cost perspective – i.e., low speed visualization is, most of the times, cheaper than high speed – , but also from a technical perspective, given that high speed visualization results in highly correlated data. Note that, however, while consecutive low speed frames are uncorrelated, they are all samples drawn from the same boiling regime, which, in this case, is nucleate boiling.

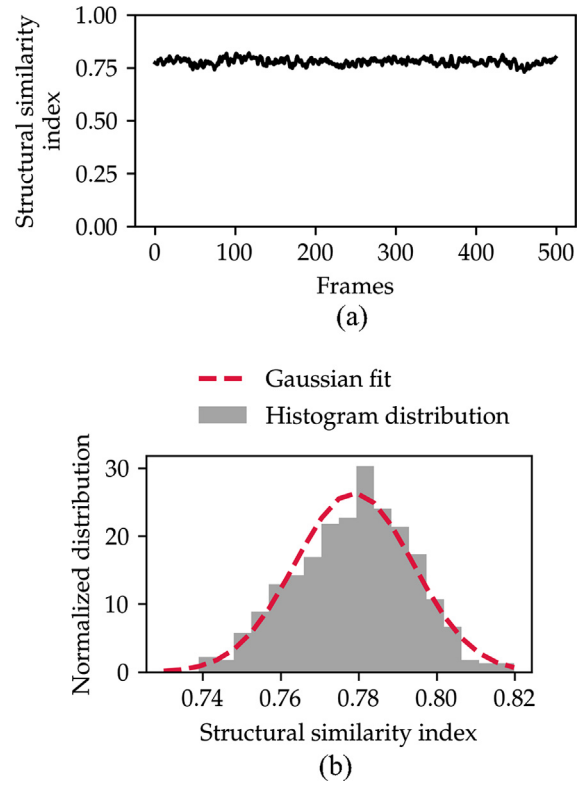

Fig. 4. (a) Structural similarity index in low speed visualization of nucleate pool boiling phenomena. (b) Structural similarity histogram for low speed visualization of nucleate pool boiling.

5. Dimensionality reduction and feature selection

In general, a RGB image frame can be described by $3N_p$ degrees of freedom, where N_p is the number of pixels, and the multiplying constant 3 characterizes the number of degrees of freedom each pixel has (i.e., the red, green and blue intensities). However, given that the concern is not in identifying colors, but in identifying boiling regimes by bubble behavior, the number of degrees of freedom can be immediately reduced threefold and becomes N_p by converting the image to greyscale, retaining only the luminance of each pixel [36]. However, note that, for a high-resolution frame, a number of features N_p may still be prohibitively expensive to compute. If fact, it is likely that the number of features that accurately describe each pool boiling regime is much smaller than hundreds of thousands. Hence, it is worthwhile to know whether it is possible to further reduce the number of degrees of freedom.

Several measures can be used when reducing the dimensionality of data. Particularly in this paper, two of them will be used: retained variance [40] and Shannon cross-entropy [3]. Consider, for instance, a zero-mean dataset $X \in \mathcal{R}^{M \times N_p}$, where M is the number of samples in the dataset and N_p is the number of degrees of freedom of each sample (i.e., number of pixels, in this case). Then, the variance of the dataset can be written as

$$\sigma_X^2 = \mathrm{var}(X) = \frac{1}{N_p M} \sum_{i=1}^{M} \sum_{j=1}^{N_p} X_{ij}^2. \tag{3}$$

Now, define a retained variance ratio V, which computes how much of the variance a new, dimensionally-reduced dataset X' retains from the original dataset X as

$$V = \frac{\mathrm{var}(X')}{\mathrm{var}(X)}. \tag{4}$$

Naturally, when performing dimensionality reduction, the goal is to maintain V as close as possible to unity in order to retain most of the original dataset variance.

In order to calculate the cross-entropy between two images, first a statistical distribution of their luminance is evaluated from a frequency histogram where each bin of the histogram corresponds to a luminance range. Then, the cross-entropy is calculated from the luminance frequency histograms of an image x and its downsampled counterpart x', i.e., let $h_x^{(N)}(L)$ be the N-bins probability histogram of the luminance L of x, then the cross-entropy ratio between x and x' can be written as

$$\frac{S(x,x')}{S(x,x)} = \frac{\int_{-\infty}^{\infty} h_x^{(N)}(L) ln[h_{x'}^{(N)}(L)] dL}{\int_{-\infty}^{\infty} h_x^{(N)}(L) ln[h_x^{(N)}(L)] dL}. \tag{5}$$

The cross-entropy generally increases as the dimensionality of the data is reduced because information is lost. Similarly, it is therefore desirable to maintain the cross-entropy ratio as close to one as possible.

5.1. Dimensionality reduction by downsampling

The first kind of dimensionality reduction that will be considered in this paper is downsampling by locally averaging neighboring pixels [36]. Downsampling is an effective tool in dimensionality reduction because it is capable of retaining a large amount of variance while significantly reducing the number of dimensions. Consider, for instance, that a downsampling factor f_{ds} is applied on the original dataset X, which corresponds to locally averaging every f_{ds} pixels in height and width, and hence reducing the number of degrees of freedom by f_{ds}^2. Fig. 5a shows that the downsampling is able to retain the variance fairly well up to very large values of downsampling factors (i.e., 50). At such high downsampling factor, the resulting number of pixels is only 160 (i.e., 8 by 20) compared to the near-million pixels in a 720p greyscale image. The reason why downsampling preserves variance well is associated with the fact that downsampling locally averages pixel luminance values, and adjacent pixels usually have fairly similar luminance.

Despite preserving variance, information is lost by downsampling, which can, in turn, be measured by Shannon cross-entropy. The cross-entropy ratio is shown in Fig. 5b, where it is plotted as a function of f_{ds}. Note that the cross-entropy increases along with f_{ds}, given that information is lost. However, for $f_{ds} < 7$, the cross-entropy ratio remains relatively constant, after which it increases significantly. Therefore, it is safe to assume that downsampling can occur without significant loss of information as long as $f_{ds} < 7$. Note that, from Fig. 5a, the variance is mostly maintained for this range. Consequently, the rest of the paper will employ a downsampling factor of $f_{ds} = 5$, resulting in a 25-fold reduction in the number of degrees of freedom. For instance, the direct observation frames are reduced from 600 by 900 pixels to 120 by 196 pixels. Therefore, for a 720p RGB image, this simple analysis would reduce the number of degrees of freedom from 2,764,800 to 961,600 (color to gray scale) and then to 36,864 (downsampling), i.e., a total 75-fold dimensionality reduction. However, that number may still require a prohibitively large amount of data to find a suitable boiling regime identification hypothesis.

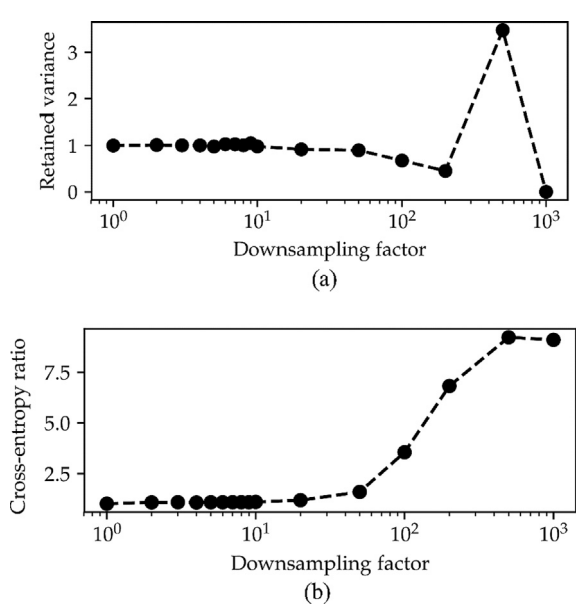

Fig. 5. (a) Pixel luminosity variance and (b) cross-entropy as a function of the downsampling factor.

5.2. Dimensionality reduction by principal component analysis (PCA)

Dimensionality reduction can be interpreted as transforming the original dataset $X \in \mathcal{R}^{M\times N}$, where M is the number of samples and N is the number of original features (i.e., pixels, in this case), into a $X' \in \mathcal{R}^{M\times K}$ dataset, where $K < N$ is the number of resulting features. Ideally, $K << N$ with minimal loss of information with respect to the original dataset – for instance, it is desirable that most of the original variance be preserved.

To accomplish that, a statistical technique known as principal component analysis (PCA) will be used. This method projects the data (i.e., low resolution frames) onto a vector space that maximizes retained variance [40]. The basis of the vector space is composed by the eigenvectors of the covariance matrix of the dataset X. In order to reduce the dimensionality of the data, the first K eigenvectors that retain the most variance are chosen to project the dataset, whereas the rest are discarded. Note that each eigenvector lies in a N-dimensional vector space. Hence, for the present case, each eigenvector can be viewed as an image of the same resolution of the frames composing the dataset X. In fact, in the field of computer vision, the eigenvectors of a PCA are often referred to as eigenfigures or eigenfaces [40,41], where each eigenfigure identifies different features of an image.

This interpretation of PCA eigenvectors can be more directly understood in mathematical terms as follows. Let ${}_i\lambda$ be the i-th eigenvector, $\Lambda \in \mathcal{R}^{N\times K}$ be a matrix of eigenvectors – where each column is an eigenvector – which, when multiplied by a data point yields

$$X'_i = {}_i\lambda^T x = \sum_{j=1}^{N} {}_i\lambda_j x_j = \sum_{j=1}^{N} \Lambda_{ji} x_j \tag{6}$$

Hence, the multiplication ${}_i\lambda_j x_j = \Lambda_{ji} x_j$ corresponds to the contribution of the j-th pixel to the i-th component of the transformed data. If ${}_i\lambda_j \approx 0$, then the contribution of the j-th pixel to the i-th component is negligible. Therefore, following the mathematics of Eq. (6), the eigenvectors – or eigenfigures – can be interpreted as masks onto which the original frames are weighted.

This procedure can be better understood as follows. Fig. 6 shows the variance that each component, i.e., eigenvector, explains and the cumulative explained variance over the first K components as a function of K. For direct observation, almost 15% of the variance is explained by the first component, and the explained variance decays quickly with the component number, as shown in Fig. 6a. It is clear that the cumulative explained variance should approach one asymptotically, but increases to nearly 1 with a relatively small number of components. In fact, this behavior is observed in Fig. 6b, where the cumulative explained variance is plotted as a function of the number of components. For indirect observation, on the other hand, the variance explained by the first components is much smaller (i.e., lower than 2%), as shown in Fig. 6c. Nonetheless, similarly to direct observation, the cumulative explained variance approaches unity asymptotically – see Fig. 6d. Hence, from over 20 thousand degrees of freedom after downsampling, only approximately 500 features are sufficiently capable of retaining over 90% of the original variance of the data for both direct and indirect observation, confirming that $K << N$.

Given that, for direct observation, the first principal eigenfigures represent the data much better than higher ones – i.e., see Fig. 6a –, it's worth exploring what they look like when viewed as frames. Recall that it is possible to visualize each eigenfigure as an image. Hence, the first, second, 200th and 500th most significant eigenfigures for direct observation are illustrated as the left frames of Fig. 7, qualitatively. Note that the first eigenfigure, Fig. 7a, largely ignores the presence of the wire and weighs the presence of bubbles in the background. The presence of bubbles

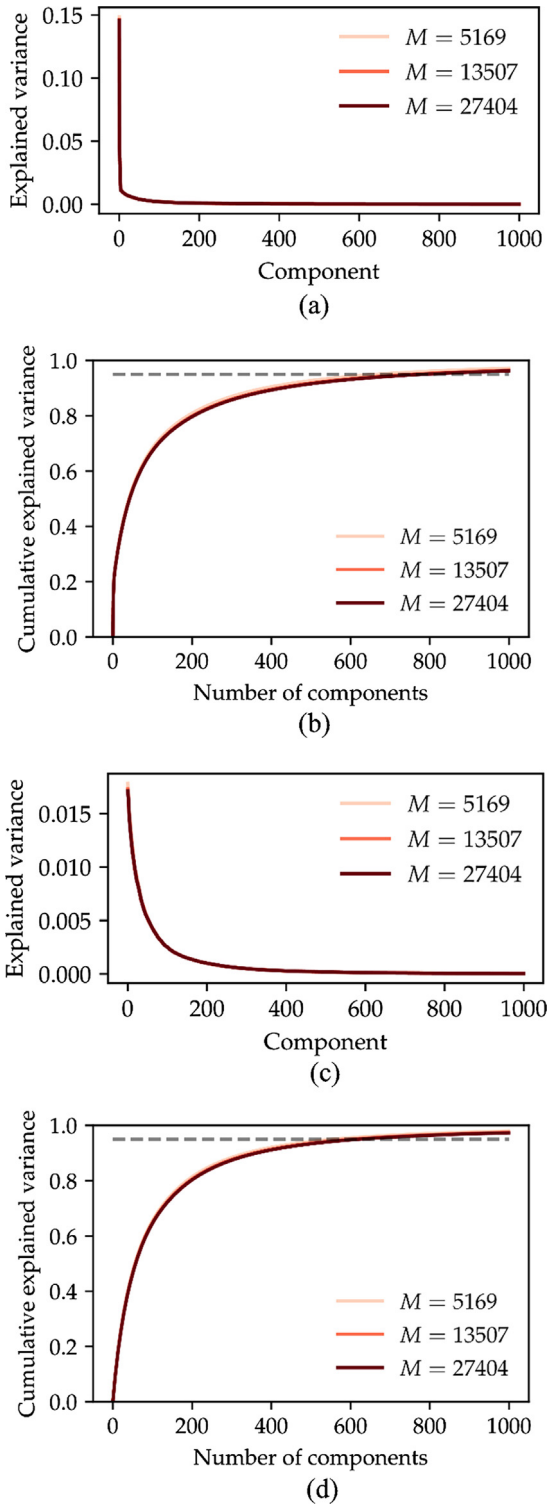

Fig. 6. (a) Component-wise explained variance and (b) cumulative explained variance as a function of the component number for various training set sizes for direct observation. (c) Component-wise explained variance and (d) cumulative explained variance as a function of the component number for various training set sizes for indirect observation.

indicates whether natural convection is occurring. The second eigenfigure, Fig. 7b, on the other hand, places some weight on the wire, and not far from it. This observation provides evidence that the PCA algorithm is capable of identifying that a large part of the variance of the dataset is due to information that is present near the wire, possibly due to bubble dynamics.

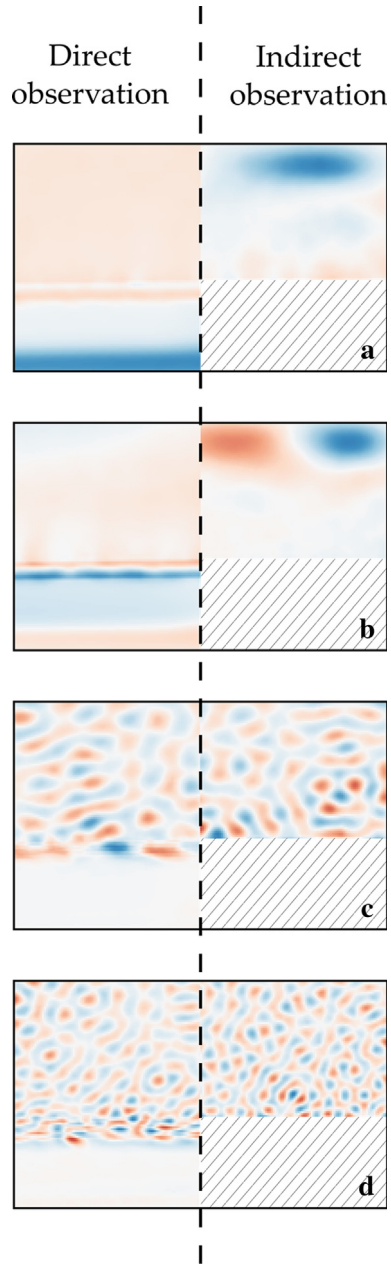

Fig. 7. (a) First, (b) second, (c) 200th and (d) 500th most significant eigenfigures obtained by principal component analysis on direct observation (left) and indirect observation (right). In red are negative values and in blue are positive values.

Finally, less significant eigenfigures appear to identify bubble structural size. In fact, the less significant the eigenfigure is, the smaller the coherent structure size it identifies. This is in accordance with both fluid mechanical theory of turbulence, for which smaller eddies tend to affect less the overall flow, as well as with information theory, as the less significant eigenfigures will attempt to detect what can be understood as almost pure noise. Particularly with respect to boiling heat transfer, the bubble departure size is usually related to larger wall superheating, and hence larger heat fluxes [31]. Hence, given that the dataset contains frames through the entire boiling curve, from natural convection to film boiling, it is expected that the structural bubble size will carry some of the variance of the dataset. Additionally, it can be numerically verified that the sum of the components of each eigenvector is zero [40]. Hence, the presence of a bubble or any other structure will disturb

the balance, increasing the contribution of a given eigenfigure. For instance, the presence of a large bubble, when masked by a high eigenfigure such as in Fig. 7c or d, will likely encompass so many small-scale structures that the contribution of the high eigenfigure with respect to large bubbles will be small. With respect to indirect observation (right frames of Fig. 7), the first eigenfigure attemps to keep track of incoming jets and columns emerging from the wire. More importantly, however, is that significant weight is placed on the top of the frame, instead of the bottom, where the wire supposedly is. This behavior is also observed in higher eigenfigures in direct observation and also in most of the first few eigenfigures of indirect observation, although not directly shown for the sake of brevity. More in-depth similar analyses of unsupervised learning algorithms – such as the PCA – may reveal important information about bubble dynamics in boiling processes.

Eigenfigures can be interpreted as being masks that weigh the frames by recalling that the multiplication ${}_i\lambda_j x_j = \Lambda_{ji} x_j$ corresponds to the contribution of the j-th pixel to the i-th component of the transformed data – see Eq. (6). Fig. 8 shows a randomly selected pool boiling frame with its pixel intensities weighted by the eigenfigures and Fig. 9 shows a randomly selected film boiling frame weighted by the eigenfigures in both direct (left side) and indirect (right side) observations.

Note that, in direct observation, when evaluating the first two most significant eigenfigures – particularly the second –, the negative (red) pixels are much more present in the nucleate boiling regime than in the film boiling regime. Additionally, as suggested by Fig. 7b, the second eigenfigure searches for symmetry on both sides of the wire. If the wire is symmetric, then the weighted pixels around the wire should roughly sum up to zero. If the bubble dynamics around the wire is asymmetric, on the other hand, then there is a non-negligible, non-zero sum around the wire. Note that asymmetric bubble dynamics is a strong indicator of Taylor instabilities occurring near the wire, as can be observed in Fig. 9a. On the other hand, the randomly selected nucleate boiling frame shows smaller bubbles that produce to the other side of the wire. This phenomenon can be observed in Fig. 8a and c, where symmetry is more evident.

Stronger and smaller-sized on-wire bubble dynamics is also observed to significantly affect higher components. Note, for instance, that the resulting weighted frames for nucleate boiling for the 200th and 500th most significant eigenfigures place some stronger weight on wire dynamics (Fig. 8d and e), whereas the weights are almost negligible for film boiling (Fig. 9d and e).

With respect to indirect observation, as shown in Fig. 7 and as previously discussed, the eigenfigures more starkly evaluate the top of the frame. An explanation as to why this happens is mostly still due and subject to future investigations, but an analysis of randomly selected nucleate and film boiling frames from Dataset 3, i.e., the right side of Figs. 8 and 9, respectively, may be of assistance. Note that due to the large bubble size, longer distances from departure to detection may be necessary to identify the unique periodic structure of the Kelvin-Helmholtz instability that happens during film boiling.

Naturally, due to the more uniform explained variance distribution amongst the eigenfigures in indirect observation, drawing conclusions from a few eigenfigures may be misleading. However, as will be shown later in this paper, the principal component analysis and the resulting eigenfigures are sufficient to create an algorithm capable of identifying pool boiling regimes. An eigenfigure analysis was performed revealing that, similarly to the previous case of direct observation, the size of the structure of the positive-negative weights tend to decrease for higher components. In fact, as $K << N$, it is likely that high eigenfigures will resemble noise and may hold little additional information during the dimensional transformation.

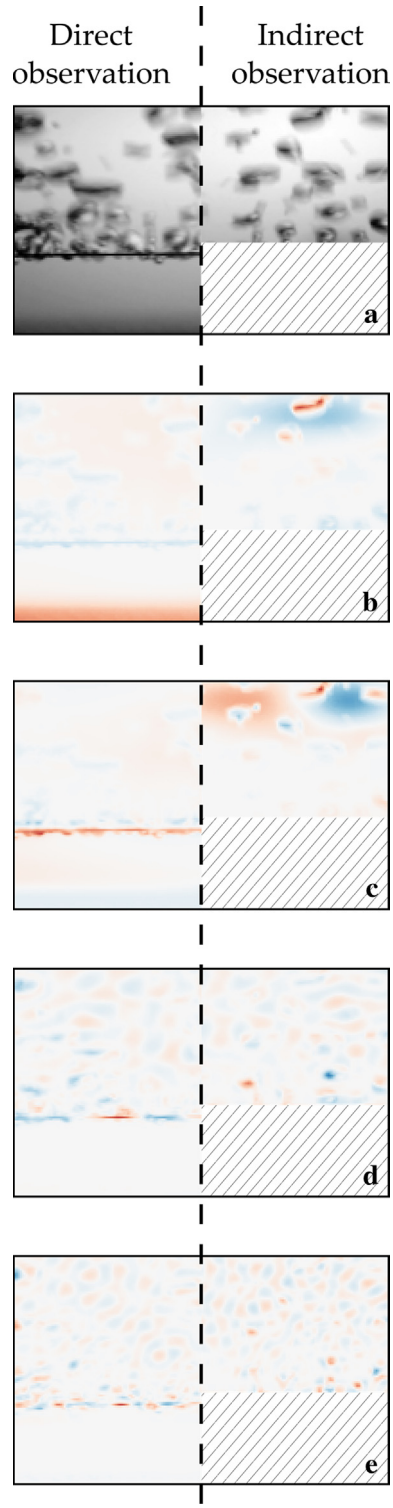

Fig. 8. (a) Random nucleate boiling frame weighted by the (b) first, (c) second, (d) 200th and (e) 500th most significant eigenfigures obtained by principal component analysis on direct observation (left) and indirect observation (right). In red are negative values and in blue are positive values.

Finally, this section concludes the dimensionality reduction of pool boiling image data. For all classification algorithms that will be presented in Section 7, the original frames are acquired at 30 Hz and 720p by a conventional DSLR camera (i.e., see Section 2). Then, the image is converted to greyscale, resulting in a threefold dimensionality reduction. The image is then cropped to remove

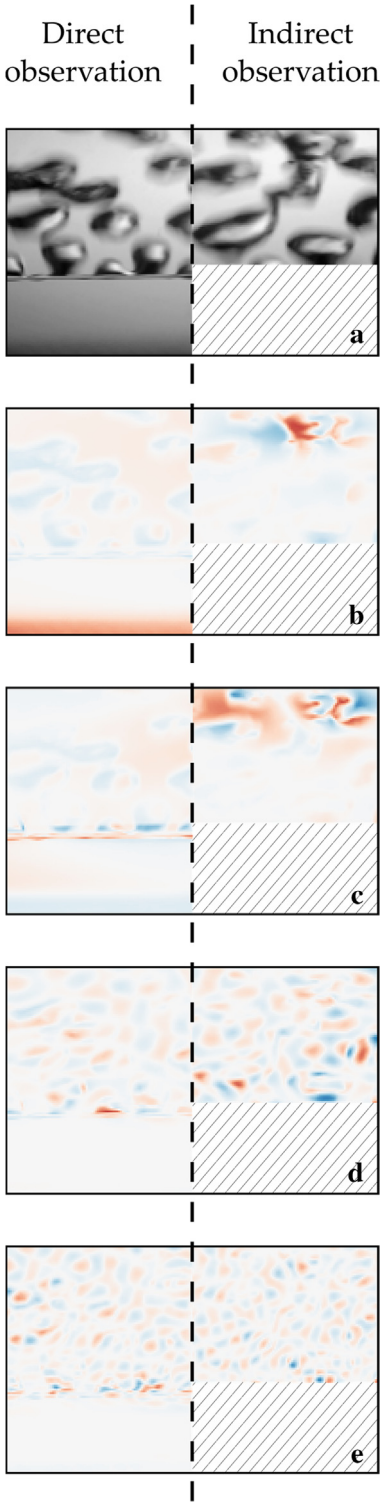

Fig. 9. (a) Random film boiling frame weighted by the (b) first, (c) second, (d) 200th and (e) 500th most significant eigenfigures obtained by principal component analysis on direct observation (left) and indirect observation (right). In red are negative values and in blue are positive values.

unnecessary background (i.e., copper electrodes). Then, each frame is downsampled by locally averaging its pixels by a factor of $f_{ds} = 5$. Then, the entire dataset is divided into two, i.e., the training set and the test set. Then, a PCA is performed on the training set in order to find the K most significant eigenfigures onto which the entire dataset is projected. In this paper, $K = 500$ retains roughly 95% of the dataset variance for all datasets, and hence is selected as the low-dimensional space. All those operations are performed on Datasets 1 through 4 – see Figs. 1 and 3. Hence, note that while the initial number of degrees of freedom was in the order of millions for the RGB 720p frame, it was possible to reduce the dimensionality of the data to $K = 500$.

While PCA could have been applied directly to the original, full resolution frames, the analysis presented in Section 5.1 is necessary to show that low resolution image data can be used to successfully train machine learning algorithms to classify pool boiling regime data, even in spite of the small scale, fast, transient bubble dynamics.

6. Dataset visualization

One of the benefits of dimensionality reduction, and in particular of using PCA, is that it enables easy dataset visualization. In fact, it is virtually impossible to visualize data in a high N-dimensional space. However, if the data is projected on to a much lower-dimensional space, such as on 2- or 3-dimensional spaces, then the dataset can be easily visualized on a traditional x–y plot figure.

Consider, for instance, Dataset 1 – direct observation with all frames. The entire dataset is projected on its first two principal components in order to facilitate data visualization, which is then shown on Fig. 10a. Note that film boiling, nucleate boiling and natural convection data appear to be easily separable, and almost linearly so, even if considering only two principal components. Another interesting feature of this demonstration is that there

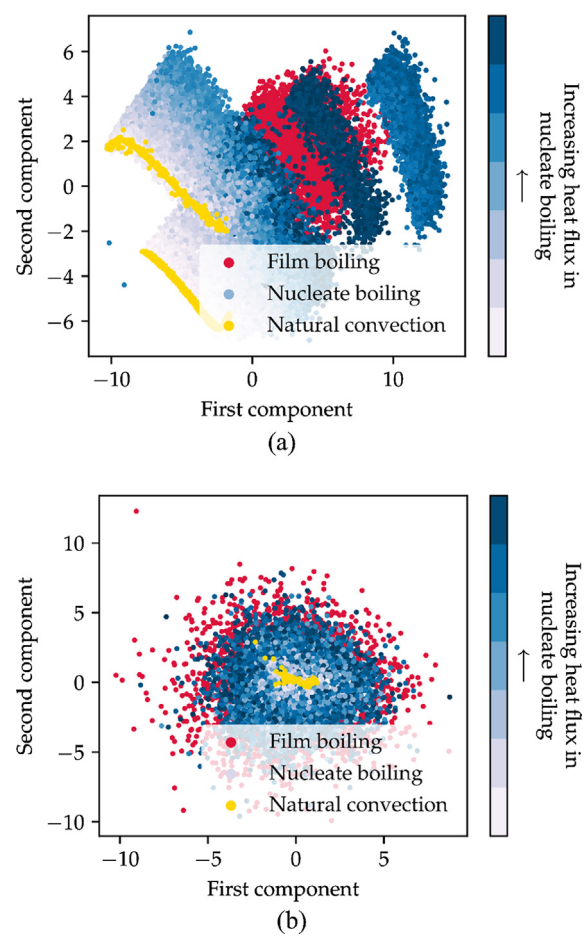

Fig. 10. Two-component PCA decomposition of (a) Dataset 1 (direct observation) and (b) Dataset 3 (indirect observation).

seems to be a particular direction along which the nucleate boiling heat flux appears to be increasing.

Consider, now, Dataset 3 – i.e., indirect observation with all frames – shown in Fig. 10b. Unlike Dataset 1, the decomposition into the two first components does not allow a clear identification of each regime. More specifically, it can be seen that the regimes are identified by Gaussian-like distributions centered at the same point, but with slightly different bandwidths. This observation indicates that it may be significantly more difficult to effectively identify the regimes with indirect observation than with direct observation, which is of course related to the fact that the first two eigenfigures in indirect observation carry little variance when compared to direct observation – see Fig. 6. Note, however, that similarly to direct observation, there is a clear direction – in this case, radial – along which nucleate pool boiling heat flux appears to increase.

7. Classification of boiling regimes

Now that some insight has been given into how the dataset behaves with respect to its principal features, a supervised classification of pool boiling regimes will be presented. The goal of this section is to apply well-known machine learning algorithms and techniques to successfully identify natural convection, nucleate boiling and film boiling regimes. The algorithms are trained on train data, which comprise 70% of the dataset, and evaluated on test data, which comprise the remaining 30%. The machine learning algorithms that will be used in this section – as well as the unsupervised learning algorithms used in the previous sections – are implemented in scikit-learn, a Python module for machine learning applications [37].

The first subsection will be dedicated to a simple classifier – i.e., the support vector machine (SVM). Then, it will be shown that the SVM has limitations with respect to the functions that it is able to learn, particularly regarding indirect observation. To overcome this issue, a neural network classifier is reported, particularly focusing on pool boiling regime classification with indirect observation. In this section, recall that the number of features (i.e., eigenfigures) is chosen to be $K = 500$, which is sufficiently large so that roughly 95% variance is retained in all datasets (Fig. 6).

7.1. Classifier performance evaluation

Several metrics have been established to evaluate the performance of classifiers, the most common ones being precision, recall and accuracy [40]. The precision P is defined as the fraction of the test set that the classifier correctly predicts (i.e., the number of true positives divided by the total number of positive identifications). The recall R is defined as the fraction of all positives that the algorithm is able to predict. The accuracy is the ratio of correct classifications.

Naturally, the ideal scenario would be to find a learning algorithm that correctly classifies the entire test set, which would in turn lead to 100% recall, precision and accuracy. Such goal is not generally achievable and, hence, most classifiers have recall and precision that are less than one. Additionally, when choosing a classifier, there is usually a compromise between precision and recall. In fact, devising an algorithm with 100% recall or 100% precision is not difficult. For instance, if we had an algorithm that classified every frame as film boiling, film boiling recall would be 100% – given that it would correctly classify all true film boiling frames as film boiling – but its precision would be small and hence it would be a poor classifier.

Additional metrics have been devised in order to accommodate the compromise between precision and recall. For instance, the F-score, which according to [40], is defined as

$$F = 2\frac{PR}{P+R}. \tag{7}$$

The F-score is the harmonic mean between precision and recall, and hence is zero whenever either the precision or the recall is zero. Additionally, the F-score is maximum (i.e., unitary) only if both the precision and the recall are also unitary and is always lower than the arithmetic mean and hence a more conservative metric than $(R + P)/2$.

In machine learning, the aforementioned metrics are usually evaluated as a function of the training set size, or the number of iterations, resulting in what is commonly referred to as the learning curve. In the training curve, the scores are plotted as a function of the training set size for both the training set and the test set – which, as previously mentioned, refer to 70% and 30% of the entire dataset, respectively. The training set scores tend to decrease as the training set size increases and the test set scores tend to increase. Ideally, for a sufficiently large training set size, the scores of both sets should be the same.

7.2. Support vector machines (SVMs)

Support vector machines (SVMs) are a class of classifiers that rely on finding a small number of points on the dataset (i.e., support vectors) that can create a dividing boundary – namely the decision boundary – in the dataset, and hence separate different classes [42] – in this case, natural convection, nucleate boiling and film boiling. The boundary generally depends on the kernel function of the SVM, which is a metric that evaluates the distance between a point and the support vectors. For instance, linear kernels can be used to classify linearly separable data. Training of the support vector machine is conducted by finding multiplicative coefficients that minimize a given cost function. More information on support vector machines can be found in various machine learning references, such as Refs. [37,40,42]. In this paper, a radial basis function (Gaussian) kernel is used with a bandwidth of $1/K$ and a unitary regularization penalty parameter. More appropriate values for those constants can be found by cross-validation, which is out of scope in this paper.

Therefore, a different SVM learner is trained for each dataset described in Section 3.1. The F-score learning curves for Dataset 1 and Dataset 3 – i.e., all data with direct and indirect observation, respectively – are shown in Fig. 11, where the training score is evaluated on the training dataset and the test score is evaluated on the test dataset. Note that the F-scores remain relatively constant after a small number of training examples. Except for natural convection identification, the F-scores are higher than 0.95 for direct observation and higher than 0.8 for indirect observation. The resulting F-scores on the test dataset after training through the entire training dataset are shown in Tables 1 and 2 for direct and indirect observation, respectively.

The low scores in natural convection identification are due to the fact that, at low heat fluxes, pool boiling occurs in very isolated nucleation sites. This issue can be easily resolved by training the algorithm without low heat flux nucleate boiling images. In fact, it was verified that using Dataset 2 and Dataset 4, the F-score of natural convection becomes unitary in both direct and indirect observation. Also, special attention should be given to the behavior of the training and test learning curves in Fig. 11b, where the training score decreases as more training examples are added while the test score increases. The present asymptotic behavior suggests that the hypothesis space through which the support vector machine searches will probably not yield much better results even if more data is included.

In order to exemplify the performance of the SVM classifier, Fig. 12a shows a collection of frames classified in the Dataset 1

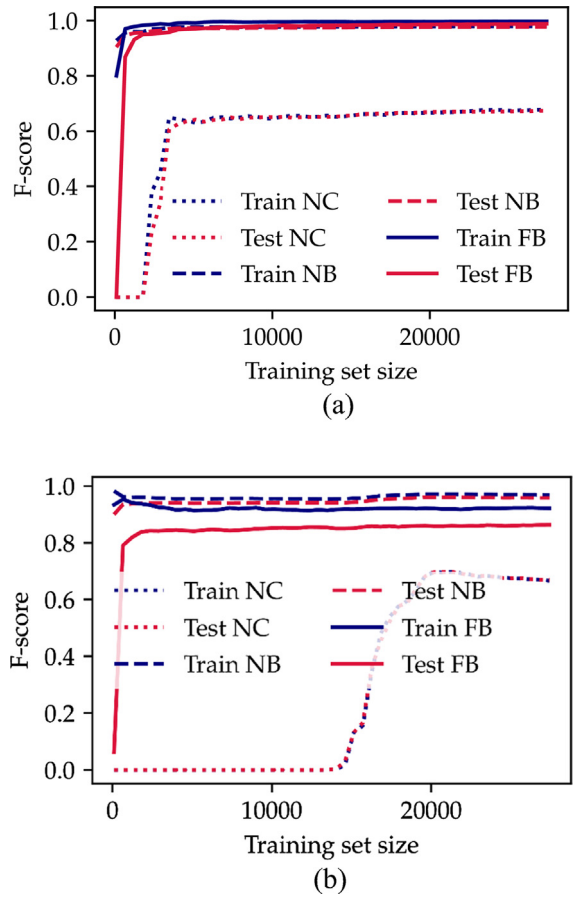

Fig. 11. Support vector machine learning curves for (a) direct and (b) indirect observation.

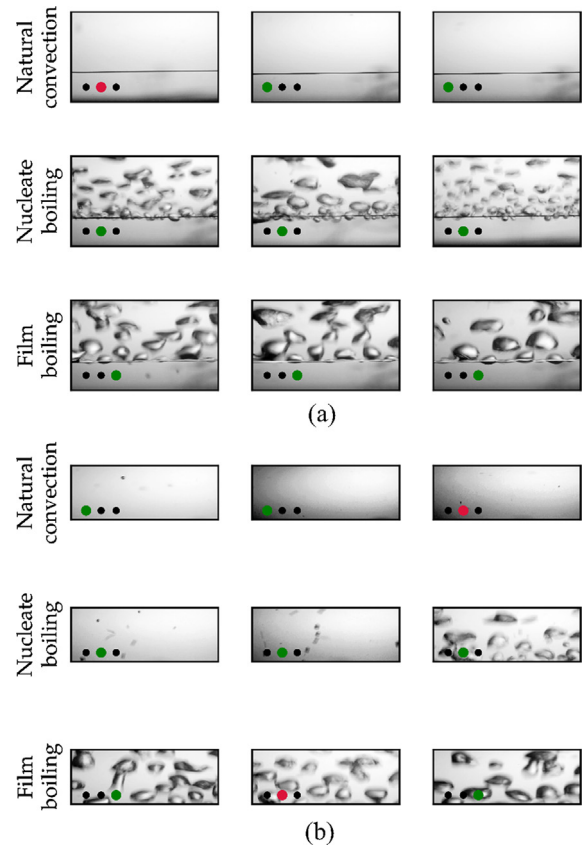

Fig. 12. Examples of classification results from the trained support vector machine on (a) Dataset 1 (direct observation) and (b) Dataset 3 (indirect observation).

Table 1
Support vector machine test scores after training through the entire training set of Dataset 1 (direct observation).

	Precision	Recall	F-score	Accuracy
Natural convection	0.8209	0.5709	0.6735	0.9624
Nucleate boiling	0.9664	0.9889	0.9775	
Film boiling	0.9882	0.9892	0.9887	

Table 2
Support vector machine test scores after training through the entire training set of Dataset 3 (indirect observation).

	Precision	Recall	F-score	Accuracy
Natural convection	0.8277	0.5627	0.6699	0.9308
Nucleate boiling	0.9456	0.9710	0.9581	
Film boiling	0.8655	0.8607	0.8631	

and Fig. 12b shows a collection of frames classified in the Dataset 3. The three markers in the bottom left corner of each frame represent the classification resulting from applying the trained SVM, whereas each row title indicates the true label of each frame. For instance, first frame occurs during natural convection but is mistakenly classified as nucleate boiling by the SVM. On the other hand, the last frame happens during film boiling and is correctly classified by the SVM.

7.3. Artificial neural networks (ANNs)

Artificial neural networks (ANNs) are a class of learning algorithms composed of several layered connected units, which are known to be able to simulate complex non-linear hypotheses and are particularly effective for classification. While many ANN architectures exist, in this paper, a simple shallow multi-layer perceptron neural network (MLPNN) is employed [43]. In this model, the features, which are the input to the neural network, compose the first layer. A second layer, often referred to as hidden layer, has U units and is connected to the first layer and to the output layer, the latter which reveals the classification assigned by the neural network. In general, a neural network may have any number W of hidden layers. The connections between units – or neurons – weight the incoming data, and each unit applies a function – known as the activation function – to the weighted data. As training data is supplied to the neural network training algorithm, the connection weights are learned. Similarly to SVMs, neural networks may suffer from overfitting, particularly if the total number of units is too large. Overfitting can be avoided by regularization.

The ANNs trained in this section assume $U = K$ with a single hidden layer – i.e., $W = 1$, and hence is a shallow multi-layer perceptron neural network. Training occurs with a cross-entropy cost function by backpropagation with a rectified linear unit activation (ReLU) [3,37,43] and a penalty coefficient of 10^{-4}. It is worth mentioning that a parametric analysis of the number of layers or number of units is not within the scope of this paper, but may be performed with cross-validation to further improve classification performance. The objective of this paper is to show that known classification algorithms can successfully and automatically

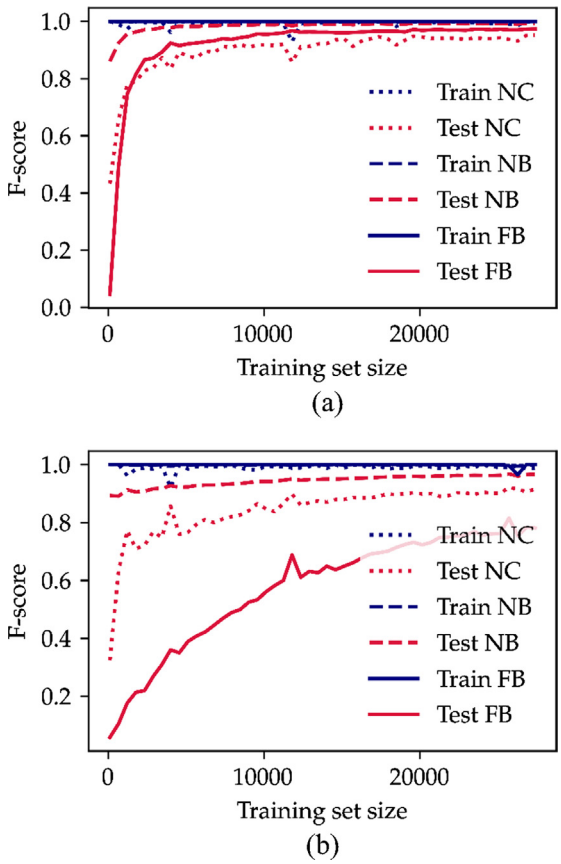

Fig. 13. Artificial neural network ($U = 500$, $W = 1$) learning curves for (a) direct and (b) indirect observation.

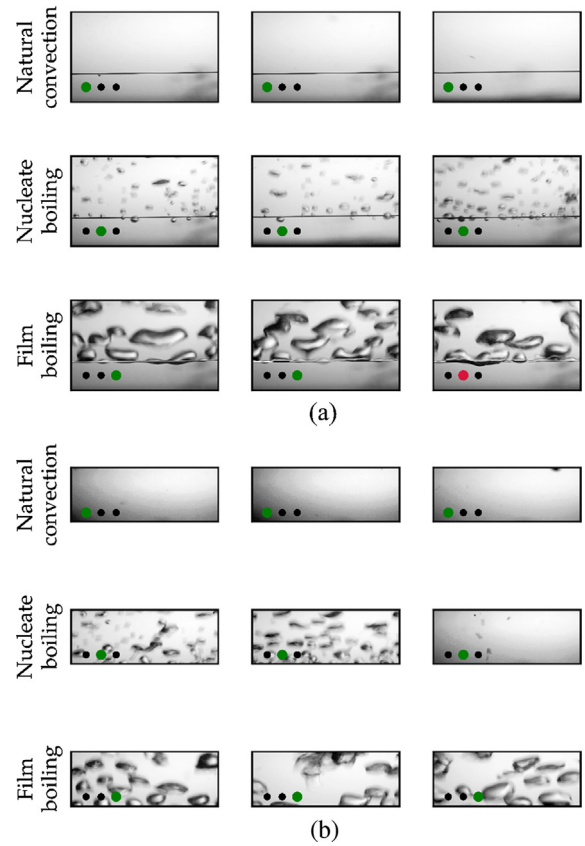

Fig. 14. Examples of classification results from the trained neural network (U = 500, W = 1) on (a) Dataset 1 (direct observation) and (b) Dataset 3 (indirect observation).

classify pool boiling regimes. An in-depth study of each algorithm can be conducted in future investigations.

The F-score learning curves for the shallow $U = 500$, $W = 1$ ANN is shown in Fig. 13 for direct and indirect observation. Note that, contrary to the support vector machine, the ANN is capable of predicting natural convection with a much higher score, both during direct and indirect observations. Additionally, the F-score for nucleate boiling is much closer to one in indirect observation using neural networks than using support vector machines. Despite having lower film boiling scores, the ANN is able to predict nucleate boiling fairly well. Tables 3 and 4 show the test scores of the ANN trained through the entire Dataset 1 and Dataset 3, respectively.

In addition, it is possible that a better neural network can be devised by performing a parametric analysis of the number of layers and number of units, along with a cross-validation with additional data, depending on the objective of the classification. Fig. 14a and b show examples of classification using neural networks for both direct and indirect observation. More importantly is the fact that even a simple shallow single-layer neural network – or even a support vector machine – can successfully classify frames acquired by direct observation automatically with over 95% recall and precision, or as much as 99% nucleate boiling precision. Over the entire test set of Dataset 1, even the shallow neural network was observed to have overall scores of 99% precision, 99% recall and 99% F-score, which is due to both the fact that the scores

Table 3
Artificial neural network ($U = 500$, $W = 1$) test scores after training through the entire training set of Dataset 1 (direct observation).

	Precision	Recall	F-score	Accuracy
Natural convection	0.9195	0.9879	0.9525	0.9883
Nucleate boiling	0.9934	0.9928	0.9931	
Film boiling	0.9929	0.9549	0.9735	

Table 4
Artificial neural network ($U = 500$, $W = 1$) test scores after training through the entire training set of Dataset 3 (indirect observation).

	Precision	Recall	F-score	Accuracy
Natural convection	0.8750	0.9587	0.9150	0.9433
Nucleate boiling	0.9534	0.9793	0.9662	
Film boiling	0.9041	0.6873	0.7809	

Note, however, that while the resulting film boiling F-score of the neural network is smaller than that of the support vector machine, that is only because its recall is much smaller, while the precision is higher.

for nucleate boiling regime classification is high and to that it composes most of the test dataset.

Furthermore, while not directly shown in this paper for the sake of brevity, a deeper neural network with $W = 10$ and $U = 500$ per layer was also observed to have an average of 99% recall, 99% precision and 99% F-score over all regimes for direct observation on the test set of Dataset 1. However, deep networks show superior scores in film boiling identification in both direct and indirect observations. These results suggest the potential in using neural networks for flow and heat transfer regime detection and classification.

A more direct comparison between support vector machines and neural networks can be observed in Fig. 15a, where the accuracy, i.e., the number of correct predictions in the test set divided by the number of samples, is shown for SVMs and NNs for both direct and indirect observation. Note that the accuracy is higher than 90% for all cases, which can also be interpreted from Tables 1–4, and as high as 98.8% for neural networks under direct observation. Recall, however, that the test set contains more nucleate boiling samples than natural convection and film boiling samples, and hence accuracy score may be biased towards nucleate boiling identification.

The similarity between the classification scores between different algorithms and for both direct and indirect observation suggests that both SVM and NNs can be used for pool boiling regime classification, although NNs have a larger number of parameters that can be explored to boost classification performance. Another important classifier metric to investigate is the time taken per prediction. The execution time per prediction for the entire test set (i.e., 9135 samples) determined by running the prediction for all test samples 10 times, where it was determined that the average time taken per evaluation is shown in Fig. 15b. Note that not only the accuracy of neural networks is higher, but the computing time is lower. Nonetheless, even for SVM, the time per prediction is sufficiently low to be indicative that both methods could be coupled to real-time pool boiling regime identification. Calculations were performed on a personal computer (Intel i7 4790 3.60 GHz, 16 GB RAM) using scikit-learn 0.19 [37] and Python 3.6.0, and do not include the time taken for projecting the frame onto the principal components.

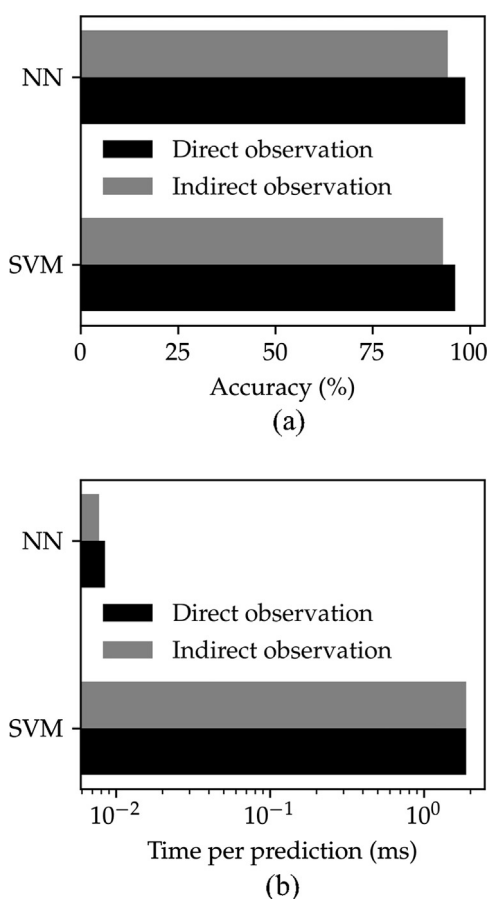

Fig. 15. (a) Accuracy score and (b) execution time per prediction on the test set for direct and indirect observation, using support vector machines (SVMs) and single hidden layer neural networks (NNs).

8. Conclusion

The present paper demonstrated that fast indirect and non-intrusive boiling regime classification is possible by low-resolution, low-speed image acquisition using simple machine learning and image processing techniques. While most boiling studies rely almost exclusively on heat flux and heater temperature data, machine learning algorithms are shown to be able to predict pool boiling regimes even in the absence of thermo-hydraulic data.

First, it was demonstrated that low frequency video acquisition – in contrast to the high speed imaging usually employed in multiphase flow investigations – are necessary for applications in machine learning techniques for boiling regime identification. Even though the present paper did not focus on boiling heat transfer physics, it is expected that the machine learning investigations conducted in this paper might motivate phenomenological investigations of fast, transient multiphase phenomena using machine learning and low speed visualization. These studies were, until now, only accessible with high speed visualization.

Using low speed visualization, the loss of variance and information during downsampling from a high to a low resolution image was investigated, where it was argued that high resolution imaging is an unnecessary – and potentially expensive – attribute for machine learning applications in pool boiling systems. Principal component analysis on the acquired frames is shown to be able to identify key features in the pool boiling phenomena, such as on-wire bubble dynamics and bubble size, as well as reduce image dimensionality for easier data visualization. Future machine learning studies involving boiling heat transfer should make efforts to reduce the dimensionality of image data.

Then, classifiers are trained on the low-speed, low resolution data, where it is demonstrated that both support vector machines and neural networks can successfully identify pool boiling regimes with over 90% accuracy even when the heater is not visible in the visualization window, and with as much as 99% precision, recall and accuracy when it is.

Finally, although simple algorithms were verified to yield promising results in pool boiling regime classification, it is expected that more complex and especially-design neural networks, such as convolutional neural networks, can further increase the accuracy of pool boiling regime identification. Moreover, while the techniques presented in this paper were implemented for pool boiling visualization, it is surmised that regime identification can be performed by a machine in other multiphase flow systems, such as during flow boiling, condensation and air-water flows.

Acknowledgments

The Authors are thankful to CNPq.

Conflict of interest

None.

References

[1] M. Campbell, A.J. Hoane, F.-H. Hsu, Deep blue, Artif. Intell. 134 (1) (2002) 57–83.
[2] D. Silver, A. Huang, C.J. Maddison, A. Guez, L. Sifre, G. van den Driessche, J. Schrittwieser, I. Antonoglou, V. Panneershelvam, M. Lanctot, S. Dieleman, D. Grewe, J. Nham, N. Kalchbrenner, I. Sutskever, T. Lillicrap, M. Leach, K. Kavukcuoglu, T. Graepel, D. Hassabis, Mastering the game of Go with deep neural networks and tree search, Nature 529 (7587) (2016) 484–489.
[3] I. Goodfellow, Y. Bengio, A. Courville, Deep Learning MIT Press, Cambridge, MA, 2016.
[4] A. Krizhevsky, I. Sutskever, G.E. Hinton, ImageNet Classification with Deep Convolutional Neural Networks, in: Advances in Neural Information Processing Systems, vol. 25, 2012.
[5] A. Esteva, B. Kuprel, R.A. Novoa, J. Ko, S.M. Swetter, H.M. Blau, S. Thrun, Dermatologist-level classification of skin cancer with deep neural networks, Nature 542 (7639) (2017) 115–118.
[6] L. Zdeborova, Machine learning: new tool in the box, Nat. Phys. 13 (5) (2017) 420–421.
[7] J. Carrasquilla, R.G. Melko, Machine learning phases of matter, Nat. Phys. 13 (5) (2017) 431–434.
[8] Q. Wei, R.G. Melko, J.Z.Y. Chen, Identifying polymer states by machine learning, Phys. Rev. E 95 (3) (2017) 032504.
[9] J. Nathan Kutz, Deep learning in fluid dynamics, J. Fluid Mech. 814 (2017) 1–4.
[10] P. Lauret, C. Voyant, T. Soubdhan, M. David, P. Poggi, A benchmarking of machine learning techniques for solar radiation forecasting in an insular context, Sol. Energy 112 (2015) 446–457.
[11] I. Bright, G. Lin, J.N. Kutz, Compressive sensing based machine learning strategy for characterizing the flow around a cylinder with limited pressure measurements, Phys. Fluids 25 (12) (2013) 127102.
[12] J.R. Barbosa, A.H. Govan, G.F. Hewitt, Visualisation and modelling studies of churn flow in a vertical pipe, Int. J. Multiphase Flow 27 (12) (2001) 2105–2127.
[13] P.J. Waltrich, G. Falcone, J.R. Barbosa, Axial development of annular, churn and slug flows in a long vertical tube, Int. J. Multiphase Flow 57 (2013) 38–48.
[14] C.E. Brennen, Fundamentals of Multiphase Flow, Cambridge University Press, 2005.
[15] J.R. Barbosa, J.C.A. Ferreira, D. Hense, Onset of flow reversal in upflow condensation in an inclinable tube, Exp. Therm. Fluid Sci. 77 (2016) 55–70.
[16] H. Wu, F. Zhou, Y. Wu, Intelligent identification system of flow regime of oil–gas–water multiphase flow, Int. J. Multiphase Flow 27 (3) (2001) 459–475.
[17] H. Shaban, S. Tavoularis, Measurement of gas and liquid flow rates in two-phase pipe flows by the application of machine learning techniques to differential pressure signals, Int. J. Multiphase Flow 67 (2014) 106–117.
[18] H. Shaban, S. Tavoularis, Identification of flow regime in vertical upward air–water pipe flow using differential pressure signals and elastic maps, Int. J. Multiphase Flow 61 (2014) 62–72.
[19] T.L. Bergman, A.S. Lavine, F.P. Incropera, D.P. Dewitt, Fundamentals of Heat and Mass Transfer, seventh ed., John Wiley & Sons Inc, New York, 2011.
[20] S.M. You, J.H. Kim, K.H. Kim, Effect of nanoparticles on critical heat flux of water in pool boiling heat transfer, Appl. Phys. Lett. 83 (16) (2003) 3374–3376.
[21] D.M. Vazquez, R. Kumar, Surface effects of ribbon heaters on critical heat flux in nanofluid pool boiling, Int. Commun. Heat Mass Transf. 41 (2013) 1–9.
[22] S.M. Kwark, R. Kumar, G. Moreno, J. Yoo, S.M. You, Pool boiling characteristics of low concentration nanofluids, Int. J. Heat Mass Transf. 53 (5) (2010) 972–981.
[23] D. Ciloglu, A. Bolukbasi, A comprehensive review on pool boiling of nanofluids, Appl. Therm. Eng. 84 (2015) 45–63.
[24] S.J. Kim, I.C. Bang, J. Buongiorno, L.W. Hu, Surface wettability change during pool boiling of nanofluids and its effect on critical heat flux, Int. J. Heat Mass Transf. 50 (19) (2007) 4105–4116.
[25] H.S. Ahn, J.M. Kim, C. Park, J.-W. Jang, J.S. Lee, H. Kim, M. Kaviany, M.H. Kim, A novel role of three dimensional graphene foam to prevent heater failure during boiling, Scient. Rep. 3 (2013) 1960.
[26] S.H. Kim, G.C. Lee, J.Y. Kang, K. Moriyama, M.H. Kim, H.S. Park, Boiling heat transfer and critical heat flux evaluation of the pool boiling on micro structured surface, Int. J. Heat Mass Transf. 91 (2015) 1140–1147.
[27] M. Tetreault-Friend, R. Azizian, M. Bucci, T. McKrell, J. Buongiorno, M. Rubner, R. Cohen, Critical heat flux maxima resulting from the controlled morphology of nanoporous hydrophilic surface layers, Appl. Phys. Lett. 108 (24) (2016) 243102.
[28] K.-H. Chu, R. Enright, E.N. Wang, Structured surfaces for enhanced pool boiling heat transfer, Appl. Phys. Lett. 100 (24) (2012) 241603.
[29] S. Mori, Y. Utaka, Critical heat flux enhancement by surface modification in a saturated pool boiling: a review, Int. J. Heat Mass Transf. 108 (2017) 2534–2557.
[30] N.S. Dhillon, J. Buongiorno, K.K. Varanasi, Critical heat flux maxima during boiling crisis on textured surfaces, Nat. Commun. 6 (2015) 8247.
[31] V.P. Carey, Liquid-Vapor Phase-Change Phenomena, Hemisphere Publishing Corporation, 1992.
[32] F. Demiray, J. Kim, Microscale heat transfer measurements during pool boiling of FC-72: effect of subcooling, Int. J. Heat Mass Transf. 47 (14) (2004) 3257–3268.
[33] J. Kim, Review of nucleate pool boiling bubble heat transfer mechanisms, Int. J. Multiphase Flow 35 (12) (2009) 1067–1076.
[34] S.v.d. Walt, S.C. Colbert, G. Varoquaux, The NumPy array: a structure for efficient numerical computation, Comput. Sci. Eng., 13(2) (2011) 22–30.
[35] J.D. Hunter, Matplotlib: a 2D graphics environment, Comput. Sci. Eng. 9 (3) (2007) 90–95.
[36] S. van der Walt, J.L. Schönberger, J. Nunez-Iglesias, F. Boulogne, J.D. Warner, N. Yager, E. Gouillart, T. Yu, s.-i. contributors., scikit-image: Image processing in Python, Peer J., 2:e453 (2014).
[37] F. Pedregosa, G. Varoquaux, A. Gramfort, V. Michel, B. Thirion, O. Grisel, M. Blondel, P. Prettenhofer, R. Weiss, V. Dubourg, J. Vanderplas, A. Passos, D. Cournapeau, M. Brucher, M. Perrot, E. Duchesnay, Scikit-learn: machine learning in python, J. Mach. Learn. Res. 12 (2011) 2825–2830.
[38] W. Zhou, A.C. Bovik, H.R. Sheikh, E.P. Simoncelli, Image quality assessment: from error visibility to structural similarity, IEEE Trans. Image Process. 13 (4) (2004) 600–612.
[39] S.S. Shapiro, M.B. Wilk, An analysis of variance test for normality (complete samples), Biometrika 52 (3/4) (1965) 591–611.
[40] K.P. Murphy, Machine Learning: A Probabilistic Perspective, The MIT Press, Cambridge, MA, 2012.
[41] M. Turk, A. Pentland, Eigenfaces for recognition, J. Cognit. Neurosci. 3 (1) (1991) 71–86.
[42] Y.S. Abu-Mostafa, M. Magdon-Ismail, H.-T. Lin, Learning from Data: A Short Course, AMLBook, 2012.
[43] S. Haykin, Neural Networks: A Comprehensive Foundation, second ed., Prentice Hall, 1998.